

Journal of Astronomical Telescopes, Instruments, and Systems

AstronomicalTelescopes.SPIEDigitalLibrary.org

Supermirror design for Hard X-Ray Telescopes on-board Hitomi (ASTRO-H)

Keisuke Tamura
Hideyo Kunieda
Yusuke Miyata
Takashi Okajima
Takuya Miyazawa
Akihiro Furuzawa
Hisamitsu Awaki
Yoshito Haba
Kazunori Ishibashi
Manabu Ishida
Yoshitomo Maeda
Hideyuki Mori
Yuzuru Tawara
Shigeo Yamauchi
Kentaro Uesugi
Yoshio Suzuki
HXT Team

Keisuke Tamura, Hideyo Kunieda, Yusuke Miyata, Takashi Okajima, Takuya Miyazawa, Akihiro Furuzawa, Hisamitsu Awaki, Yoshito Haba, Kazunori Ishibashi, Manabu Ishida, Yoshitomo Maeda, Hideyuki Mori, Yuzuru Tawara, Shigeo Yamauchi, Kentaro Uesugi, Yoshio Suzuki, HXT Team “Supermirror design for Hard X-Ray Telescopes on-board Hitomi (ASTRO-H),” *J. Astron. Telesc. Instrum. Syst.* **4**(1), 011209 (2018), doi: 10.1117/1.JATIS.4.1.011209.

Supermirror design for Hard X-Ray Telescopes on-board Hitomi (ASTRO-H)

Keisuke Tamura,^{a,*} Hideyo Kunieda,^a Yusuke Miyata,^a Takashi Okajima,^b Takuya Miyazawa,^c Akihiro Furuzawa,^d Hisamitsu Awaki,^e Yoshito Haba,^f Kazunori Ishibashi,^a Manabu Ishida,^g Yoshitomo Maeda,^g Hideyuki Mori,^b Yuzuru Tawara,^a Shigeo Yamauchi,^h Kentaro Uesugi,ⁱ Yoshi Suzuki,ⁱ and HXT Team

^aNagoya University, Graduate School of Science, Division of Particle and Astrophysical Science, Furo-cho, Chikusa-ku, Nagoya, Aichi, Japan

^bNASA Goddard Space Flight Center, Greenbelt, Maryland, United States

^cOkinawa Institute of Science and Technology Graduate University, Onna-son, Kunigami, Okinawa, Japan

^dFujita Health University, Kutsukake-cho, Toyoake, Aichi, Japan

^eEhime University, Bunkyo-cho, Matsuyama, Ehime, Japan

^fAichi University of Education, Igaya-cho, Kariya, Aichi, Japan

^gInstitute of Space and Astronautical Science (ISAS), Japan Aerospace Exploration Agency (JAXA), Yoshinodai, Chuo-ku, Sagamihara, Japan

^hNara Women's University, Kitauoyanishi-machi, Nara, Nara, Japan

ⁱJapan Synchrotron Radiation Research Institute, Sayo-cho, Sayo-gun, Hyogo, Japan

Abstract. We designed depth-graded multilayers, so-called supermirrors, with platinum/carbon (Pt/C) layer pairs for the Hard X-Ray Telescope (HXT) that was on-board the sixth Japanese X-Ray Astronomy Satellite Hitomi (ASTRO-H). The HXT has multineested thin foil optics, and the grazing angles of the x-ray mirrors are 0.07 to 0.27 deg. Supermirrors for HXTs are designed to provide a broad energy response (up to 80 keV) for astronomical requests. Under practical boundary conditions, we establish a block method applying empirical rules to maximize the integrated reflectivity. We fabricated Pt/C supermirrors using a DC magnetron sputtering system. The reflectivity of the mirrors was measured in a synchrotron radiation facility, SPring-8. We describe the design method for the supermirrors and our results. © The Authors. Published by SPIE under a Creative Commons Attribution 3.0 Unported License. Distribution or reproduction of this work in whole or in part requires full attribution of the original publication, including its DOI. [DOI: [10.1117/1.JATIS.4.1.011209](https://doi.org/10.1117/1.JATIS.4.1.011209)]

Keywords: x-ray; telescope; x-ray optics; multilayer; supermirror; Hitomi (ASTRO-H).

Paper 17068SS received Aug. 18, 2017; accepted for publication Dec. 18, 2017; published online Jan. 22, 2018.

1 Introduction

In the 1960s, the observational window of astronomy was newly opened to x-rays, whose sensitivity has been dramatically improved by imaging x-ray telescopes developed in the late 1970s. A violent and fascinating universe had been revealed to include accretion onto neutron stars and black holes, hot plasma emissions of supernova remnants, interstellar media, clusters of galaxies, and so on. Because the covered energy range by early x-ray telescopes was limited to below a few or several keV owing to lower reflectivity at higher energies, emissions detected were mostly those produced by thermal phenomena. However, hard x-rays above 10 keV are produced by nonthermal phenomena with high-energy particles, active galactic nuclei, or nuclear transitions in supernova remnants. These hard x-ray characteristics were observed with nonimaging hard x-ray detectors, such as proportional counters, scintillators, and solid-state detectors. Now, imaging capability is requested of hard x-rays to examine the spatial information of diffuse sources and to obtain better sensitivity for faint point sources. Both non-x-ray backgrounds and sky backgrounds are suppressed in imaging observations.

The first step of x-ray imaging with hard x-rays involved high-throughput optics with nested thin-shell x-ray telescopes on-board ASCA¹ and Suzaku.^{2,3} This pushed the upper

bound of energy coverage up to 10 keV with grazing angles (angles measured from the mirror surface) of 0.7 deg or less. This allowed us to explore a wide variety of astrophysical objects with Fe-K emission lines at 6 to 7 keV. The key technology involves a thin (~0.15 mm) substrate of individual reflectors to enhance the aperture efficiency at small grazing angles of < 0.7 deg. Instead of polishing the surfaces, a plastic coating or replica method was used to smooth the mirror surfaces. Subsequently, the High-Energy Replicated Optics program involved balloon-borne hard x-ray observation. Extreme grazing incidence optics was utilized and covered an energy band up to 60 keV.⁴

A further step was taken by the introduction of the multilayer supermirror to reflect hard x-rays up to several tens of keV.^{5,6} Alternating layers of two different materials as thin as a few nanometers deposited on the mirror surfaces reflect hard x-rays when the spacing d of each pair and grazing angle θ satisfy the Bragg equation

$$2d \sin \theta = \lambda, \quad (1)$$

where λ is the x-ray wavelength. The reflectivity is enhanced by the interference of many boundaries of the multilayers in phase. By increasing d from the bottom to the top of the multilayer structure (depth-graded density), various wavelengths of x-rays can be reflected by part of the multilayer structure with corresponding d . This technology was originally developed for neutron optics and was named the supermirror.⁷ The supermirror provides hard x-ray reflection in broader wavebands according

*Address all correspondence to: Keisuke Tamura, E-mail: tamura@u.phys.nagoya-u.ac.jp

to its design. Because the energy of x-rays from astronomical objects ranges in a broad band, the energy response provided by the multilayer supermirror is better suited for astronomical telescopes. In one study, 10 pairs of test mirrors with supermirrors were produced and installed in an ASCA spare telescope housing. The x-ray imaging performance was confirmed by hard x-ray experiments.⁶

The first astronomical observations of hard x-ray imaging were performed by the InFOC μ S balloon experiments in 2001 and 2004.^{8–10} Hard x-ray images in an energy range from 25 to 45 keV were successfully obtained with Pt/C multilayers deposited on nested thin foil mirrors similar to those in ASCA and Suzaku. In these balloon experiments, multilayer optics technology was established, and its scientific merits were confirmed.

NuSTAR is an American satellite funded by the small satellite mission SMEX and was launched on June 13, 2012. It is the first satellite carrying telescopes with the ability to focus light in the high-energy x-ray region (5 to 80 keV). The telescopes have conical approximation Wolter-I optics with a focal length of 10 m. Pt/C and tungsten/silicon (W/Si) multilayer supermirrors are used to extend the energy band up to 80 keV.^{11,12}

The NuSTAR supermirrors were designed using a power-law method, which is similar to the method used in neutron optics. In this method, six parameters are used to optimize and achieve an energy band of up to 80 keV.

The energy band of the Hard X-Ray Telescope (HXT) onboard the Hitomi (ASTRO-H) satellite was also extended up to 80 keV using the multilayer supermirror. Its energy band is essentially the same as that of NuSTAR. Supermirrors were designed based on the InFOC μ S balloon-borne telescope. The design method for multilayer supermirrors is explained in Sec. 2.

In this paper, we focused on the design method of the supermirror for the Hitomi HXT. Total performances and calibration results of Hitomi HXT, including the effective area and the field of view against photon energy, are described in detail in other papers by Matsumoto et al.¹³ and Mori et al.¹⁴ in this special section.

2 Hitomi Hard X-Ray Telescope

The Hitomi team proposed four major science cases:¹⁵

1. Revealing the large-scale structure of the universe and its evolution.
2. Understanding the extreme conditions in the universe.
3. Exploring the diverse phenomena of the nonthermal universe.
4. Elucidating dark matter and dark energy.

To explore these cutting-edge science cases, an unprecedented spectroscopic capability and a wide-band energy coverage are required for Hitomi.

For hard x-ray imaging, high sensitivity is required to detect point sources with a brightness, that is, 100,000 times fainter than that of the Crab nebula in hard x-rays (above 10 keV). To achieve this goal, the HXT must have an effective area of 300 cm² at 30 keV, an energy range of 5 to 80 keV, angular resolution better than 1.7 arc min half-power diameter (diameter to include 50% of concentrated flux), and a field of view of ~9 arc min. Assuming a focal length of 12 m and innermost

radius of 6 cm, the grazing angle ranges from 0.07 to 0.27 deg. This paper describes how to optimize the multilayer design to satisfy the scientific requirements under the boundary conditions mentioned above.

3 Material and Fabrication Issues

3.1 Selection of Multilayer Materials

The first step in supermirror design is the selection of the materials for each layer pair. The multilayer consists of layer pairs with two different elements: heavy and light. For high reflectivity, the contrast between the refractive indices of two materials must be large, and their absorption edges should not appear in the target energy region. In addition, interfacial diffusion between two materials blurs the contrast of the refractive index at the boundaries, which is equivalent to an increase in the interfacial roughness and causes degradation of the multilayer reflectivity.

Because the refractive index δ is proportional to the electron density, high-Z elements have been used for mono- and multilayer reflectors. These elements include W, Ir, Pt, and Au. Gold (Au) has often been used for total reflection mirrors of the ASCA and Suzaku x-ray telescopes because of its chemical stability. However, an island structure is sometimes found in thin Au layers of less than a few nm. Tungsten (W) is often used for the W/C and W/Si multilayers. Although the supermirror shows reasonable performance below its K absorption edge at 69.5 keV, W cannot be our choice because we are pursuing hard x-rays up to 80 keV. Platinum (Pt) is most suitable for our purposes, because it is chemically stable and has higher (electron) density than Au. Its absorption edge at 79 keV is acceptable with respect to the high-energy end of the required energy range of < 80 keV.

For light elements, carbon (C) and Si are often used in various multilayer designs. Pt/C and Pt/Si have almost the same calculated reflectivity, but the interfacial roughness of Pt/Si was several times higher than that of Pt/C in our fabrication system. Thus, our final choice was a combination of Pt and C for our multilayers.

3.2 Fabrication of Pt/C Multilayers

The multilayer structure is created by vacuum deposition. In our case, Pt and C are sputtered using argon (Ar) with DC biases. The thickness of individual layers is controlled by the sputtering rate and deposition time. The DC bias voltage and current and the Ar pressure are controlled to maintain a constant deposition rate. For example, Ar pressure is set at 0.2 to 2.0 Pa and the bias voltage is adjusted between 500 and 900 V so that the plate current remains constant. The actual deposition rate on the sample is also determined by the distance from the sputtering target to the sample. Because the mirror sample is rotated in front of the sputtering target, the deposition time is defined by the rotation speed and the window width of a mask placed between them. The uniformity of the thickness distribution on the sample is better than 5% using a special mask pattern that is narrower in the middle and wider at both ends. This compensates for the fast deposition rate occurring in the middle of the 50-cm-long Pt and C targets.

It is well known that the reflectivity of a multilayer degrades as $\exp - (2\pi\sigma/d)^2$ when d approaches $2\pi\sigma$, where d is the thickness of one-layer pair and σ is the interfacial roughness

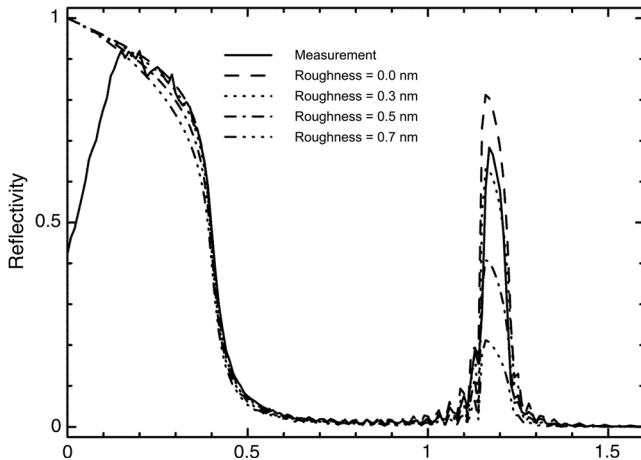


Fig. 1 Measured reflectivity of typical multilayer (Pt/C multilayer with $2d$ of 5 nm, 30-layer pairs, Γ of 0.4) comparing actual grazing angles with simulated ones having interfacial roughness σ of 0, 0.3, 0.5, and 0.7 nm.

(Debye–Waller factor). For our typical Pt/C multilayer with d of 5 nm, Fig. 1 shows simulated reflectivity curves of a typical multilayer with different $\sigma = 0, 0.3, 0.5$, and 0.7 nm. Note that interfacial roughness higher than 0.3 nm degrades the multilayer reflectivity considerably. Here, $2\pi\sigma$ approaches or becomes greater than d . The solid line in Fig. 1 is the measured reflectivity of the multilayer produced by our DC sputtering system, which indicates that we are able to achieve σ of 0.3 nm for a Pt/C supermirror.

Such σ of 0.3 nm limits the minimum d -spacing d_{\min} , as suggested above. From our experiments, the minimum d -spacing must be equal to or longer than 2.4 nm.

For the actual fabrication of the telescopes, the time we were able to spend on multilayer deposition was limited. We selected the upper limit of layer pairs as 140 for the Hitomi HXT. It was also found that σ became worse when more than 200-layer pairs were deposited. This is because the interfacial roughness accumulates and grows significantly. The upper limit of 140-layer pairs prevents performance deterioration in our design.

4 Supermirror Design for Hard X-Ray Telescopes

4.1 Boundary Conditions and Design Goals

In this section, the design scheme of the depth-graded multilayers is described for the Hitomi HXT to provide a broad response at high energy above 20 keV, under the boundary conditions set by the geometry of the mission and by the deposition technology. First, boundary conditions are listed as below based on the scientific and technical requirements:

1. multilayers of Pt and C,
2. energy range: < 80 keV,
3. grazing angles: 0.07 to 0.27 deg,
4. maximum layer pairs: 140 pairs, and
5. minimum d -spacing: 2.4 nm.

Under these boundary conditions, the goals are as follows:

1. to maximize integrated reflectivity in the required energy band and
2. to minimize the complex structure of the reflectivity profile versus x-ray energies.

In the following sections, our design scheme for the multilayers is shown step by step to optimize the multilayer parameters based on the above goals.

4.2 Top Layer

One significant difference between this design and the balloon experiment appears in the soft x-ray region below 20 keV. In such a soft x-ray region, the total reflection is dominant, so it is necessary for each supermirror design to have a reflectivity profile smoothly connected to that of the total reflection.

At a given grazing angle θ , the total reflection is effective for x-rays below the critical energy E_c . The first-layer thickness is set to be $d_{\text{Pt}0}$ (thickness of the first Pt layer) so that the x-ray at an x-ray energy of E_c will be attenuated to $1/e$ by the top layer. That is, $(d_{\text{Pt}0}/\sin \theta) \times \sigma(E_c) \times n = 1$, where $\sigma(E_c)$ is the absorption cross-section per atom and n is the number density of atoms.

In Fig. 2, the reflectivity of a supermirror with a top layer is plotted against the energy for a grazing angle of 0.25 deg. The green line indicates that a reflectivity of 5.1 nm thus derived for $1/e$ fills the dip below 20 keV and allows sufficient enhancement around 25 keV, whereas a thicker top layer, such as 7.5 nm (red line), shows a significant dip near 25 keV. Figure 3 shows the reflectivity for a grazing angle of 0.11 deg. It indicates that the top layer of 10.8 nm (green line) derived for $1/e$ is too thick, so the dip at 50 keV is significant. The red line in Fig. 3 suggests that 7.5 nm is sufficient to recover half of the dip between 30 and 40 keV. This is because the ratio of optical constants δ/β becomes larger for the E_c of 40 keV or higher, so the reflectivity below E_c may be high. Therefore, the top layer should not be thicker than 7.5 nm for small grazing angles to avoid the large attenuation of hard x-rays that would be reflected by the lower part of the multilayers. We decided to set $d_{\text{Pt}0}$ at 7.5 nm for $\theta < 0.17$ deg (Fig. 4).

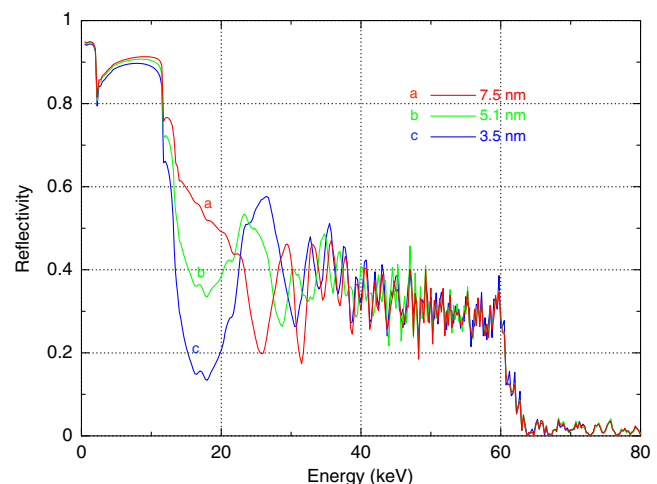


Fig. 2 Reflectivity curves at grazing angle of 0.25 deg plotted against photon energy. Red, green, and blue lines correspond to top-layer thicknesses of 7.5, 5.1, and 3.5 nm, respectively.

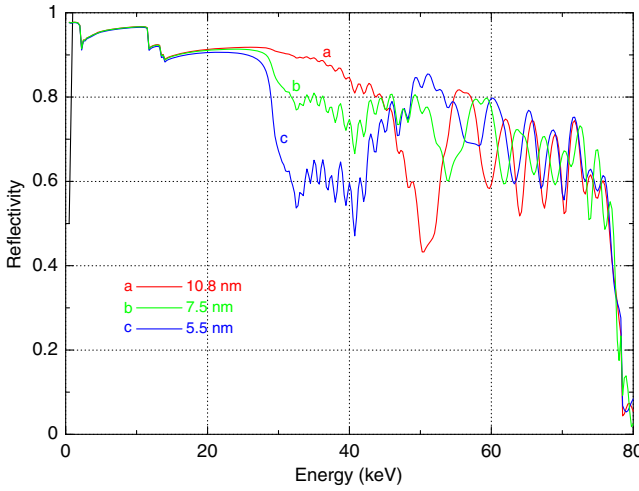


Fig. 3 Reflectivity curves at grazing angle of 0.11 deg plotted against photon energy. Red, green, and blue lines correspond to top-layer thicknesses of 10.8, 7.5, and 5.5 nm, respectively.

4.3 First Block

Under the top-layer pair, the first multilayer block with a constant d -spacing of d_1 is designed to reflect x-rays optimally at E_1 . The Bragg energy of the first block, E_1 , is defined such that $1/e$ of the incident x-ray flux can emerge from the bottom boundary of the top layer at the energy E_1 . Above $\theta \geq 0.17$ deg, the Bragg energy E_1 is equal to the critical energy E_c . However, some flux is transmitted for $\theta < 0.17$ deg and then E_1 , at which the attenuation length is ~ 7.5 nm, slightly less than E_c . Thus, d -spacing of the first block is $d_1 = hc/(2E_c \sin \theta)$ for $\theta \geq 0.17$ deg.

The reflectivity of the first block is calculated for different numbers of layer pairs (Fig. 5) at a grazing angle of 0.2 deg as a typical case for the HXT. The peak reflectivity R_p rises as $\propto N^2$ for small N , where N is number of layer pairs, and the slope gradually decreases for larger N . For higher x-ray energies, more layer pairs are necessary (smaller slope in Fig. 5),

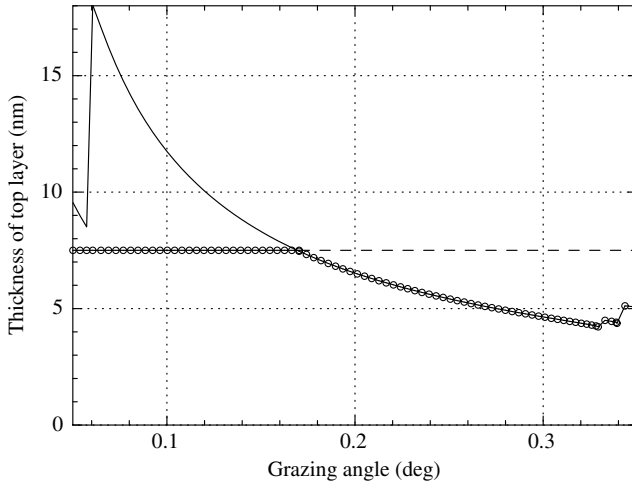


Fig. 4 Thickness of top layer versus grazing angles. Solid line shows the attenuation length of Pt. Open circle illustrates the chosen thickness of a top layer in our design. Above 0.17 deg, the Pt top layer decreases with grazing angle. Below 0.17 deg, the thickness of the top layer should be 7.5 nm to avoid strong attenuation.

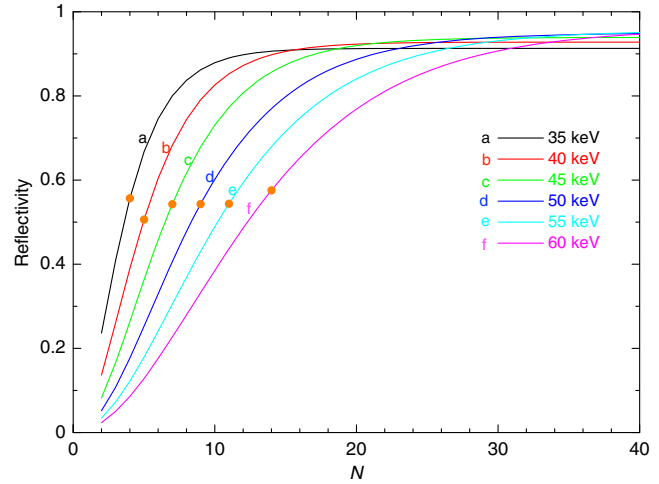


Fig. 5 Reflectivity of multilayer Bragg peak at a grazing angle of 0.2 deg plotted against the number of layer pairs N . It increases rapidly for small N and begins to saturate for large N . Curves of different colors represent reflectivity curves for different x-ray energies. Solid circles on individual lines depict the N that provides maximum integrated reflectivity ($= R_p/N$).

whereas the reflectivity is more than 90% at the saturation level for large N . At the same time, the bandwidth W of the reflectivity will become narrower as a function of $1/N(W/E \propto 1/N)$ because more layer pairs place tighter constraints on interference. Therefore, the integrated reflectivity is given as the product of the peak reflectivity R_p and the bandwidth W . Figure 6 is a plot of R_p/N , which is proportional to $R_p \cdot W$. It peaks at seven layer pairs for 45 keV, for example. Adding more than seven layer pairs does not improve the integrated reflectivity. Reflectivity peaks are marked with a solid circle in Fig. 6. In Fig. 5, the optimum layer numbers are shown with circles on curves for different x-ray energies, corresponding to the peaks in Fig. 6. They essentially correspond to 60% of the saturated reflectivity with an infinite number of layers. We calculated such optimum layer numbers for various x-ray energies, as shown in Fig. 7. Most of the data can be fitted by a straight line from 30 to 60 keV. Below 30 keV, one pair is sufficient.

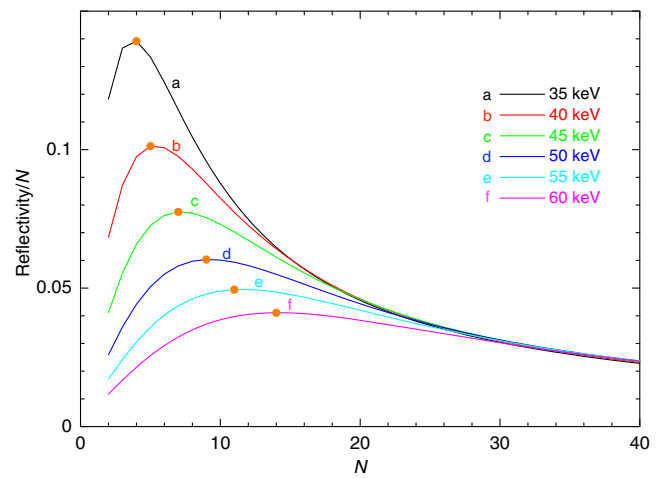


Fig. 6 Product of R_p and $1/N$ plotted against x-ray energy E . Orange circles indicate peaks of R_p/N , which correspond to the circles in Fig. 5.

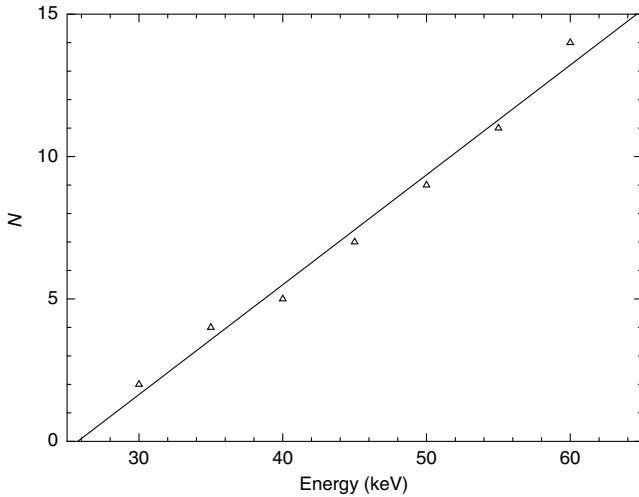


Fig. 7 Necessary layer numbers N for various x-ray energies. They are given by the peaks in Fig. 6. Straight line is best-fit linear function to the data.

Γ is the ratio of thicknesses of the heavy elements d_{Pt} to the total pair thickness d . The reflectivity of the first and second Bragg peaks depends on Γ . Because the reflectivity at the first Bragg peak becomes maximum for Γ of ~ 0.4 , this is generally used for all designs in the following part of this paper.

However, Γ of 0.5 is intentionally adopted when the second Bragg peak energy is in the energy range to be covered by the bottom layer pairs with shorter d -spacing values. This is because the second Bragg peak reflectivity becomes negligible for Γ of 0.5. In turn, this alleviates the influence of the second Bragg peak to affect the block design scheme for the first block. Note that, for the i 'th block, the same rule applies unless the second Bragg peak appears below 80 keV.

4.4 Block Method

Our basic strategy is a block method, which is characterized by blocks with constant d .⁶ Figure 8 shows the structure of the supermirror. In our design, the block contributing to the lowest

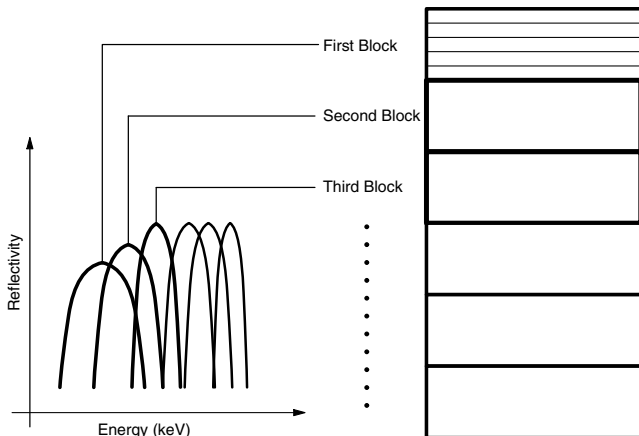


Fig. 8 Structure of supermirror designed by block method (right). The supermirror consists of multiblocks, which have a constant d spacing multilayer. The Bragg energy of each block is different, and reflectivity profile of the supermirror is determined virtually by superposition of each block.

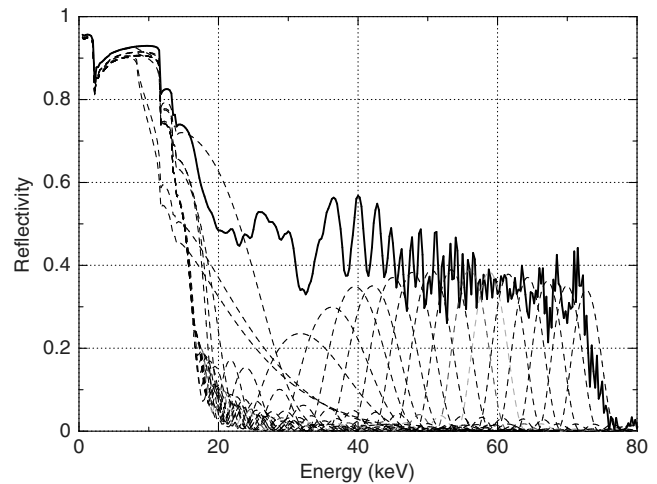


Fig. 9 Reflectivity of supermirror (solid line) and individual blocks (dashed lines) of supermirror designed for seventh group of mirror shells at incidence angle of 0.208 deg.

energy reflectance should be placed on the surface to reduce absorption. The deeper blocks contribute to the reflectance of higher energy x-rays.

As the block method consists of many parameters, d_i , N_i , and Γ_i (i is the number of blocks counted from the top), we can construct various reflectivity profiles compared with other methods.

In Fig. 9, the dashed line represents the reflectivity of each block of the multilayer at $\theta = 0.208$ deg. The solid line corresponds to the response of the supermirror with all blocks. The multilayer parameters are optimized in each block according to the scheme mentioned in Sec. 4.3. The energy steps between blocks will be determined in Sec. 4.5. In this scheme, all parameters are determined automatically without any assumed function to design the d -spacing d_i or $d(z)$ (z is the depth of the structure), which sometimes have been introduced in other research without any causality.

4.5 Energy Steps ΔE 's Between Blocks

After determining the multilayer parameters of the first block, the energy step $\Delta E (= E_{i+1} - E_i)$ to the next block must be determined. It must be smaller than the bandwidth of W_i to avoid gaps between the responses of adjacent blocks (Fig. 8). As E_i increases, the necessary number of pairs increases, but the bandwidth W_i becomes narrower, which is represented as $W_i/E_i \propto 1/N_i$. If we take into account the linear relationship between N_i and E_i in Fig. 7, N_i is roughly proportional to E_i at high energies ($N_i \propto E_i$). Therefore, the energy step to the next block of the multilayer $\Delta E (\sim W_i)$ has to be constant.

Once we assume the energy step ΔE at a certain value, it is possible to design all parameters according to the above scheme and the boundary conditions. In Fig. 10, reflectivity curves are shown for different cases of $\Delta E = 2, 3$, and 4 keV. A small ΔE of 2 keV (black line in Fig. 10), for example, has sufficient overlaps between neighboring blocks, but the energy band reaches only 60 keV. It cannot reach the upper bound of 80 keV because of the upper limit of the total number of pairs. Even if limited to no < 60 keV, no significant increase of reflectivity is apparent in the reflectivity curve. By contrast, a large ΔE of 4 keV causes gaps between neighboring blocks because ΔE is larger than the

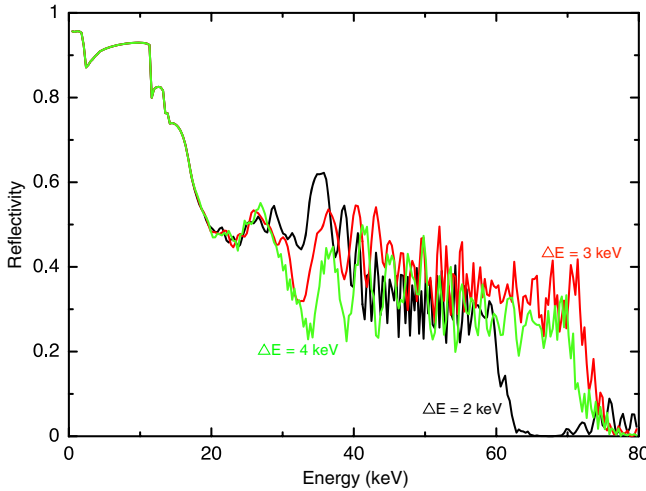


Fig. 10 Reflectivity curves of supermirrors designed with different energy steps of $\Delta E = 2$ (black), 3 (red), and 4 (green) keV.

bandwidth W_i . In Fig. 11, the integrated reflectivity is plotted against different energy steps ΔE from 2 to 4 keV. It peaks at 3 keV in this design scheme. Hence, the energy step ΔE of 3 keV is adopted for the Hitomi HXT. At a grazing angle of 0.208 deg, we need 138 layer pairs in 18 blocks spaced at 3-keV steps. Table 1 shows a set of the supermirror parameters optimized at a θ of 0.208 deg, which was actually used for the Hitomi HXT. The numbers in parentheses are the spacing d_i and the number of layer pairs N_i in the i 'th block together with Γ_i .

4.6 Grazing Angles from 0.07 to 0.27 deg

In the discussion above, a grazing angle of 0.2 deg is illustrated as a typical value to optimize the multilayer design. For the Hitomi HXT, the grazing angle ranges from 0.07 to 0.27 deg. Every set of multilayer parameters is, in principle, determined with the same design scheme. A total of 213 mirror shells are split into 12 groups so that the grazing angles of mirror shells in individual groups vary within 5% of each other. In each group, the same multilayer parameters are used for the mirror shells.

In Fig. 12, the d -spacing of the i 'th layer pair is plotted against the layer number from the surface.

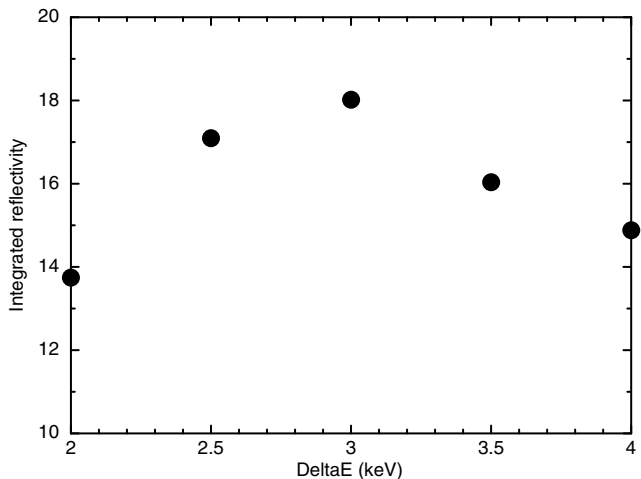


Fig. 11 Integrated reflectivity plotted against energy steps ΔE 's between blocks; obtained by integration of the reflectivity curves shown in Fig. 10.

Table 1 Supermirror parameters for grazing angle of 0.208 deg.

i	d_i (nm)	N_i	Γ_i
Top	10.6	1	0.65
1	6.67	1	0.5
2	6.00	1	0.5
3	5.45	2	0.5
4	5.00	3	0.5
5	4.62	4	0.5
6	4.29	5	0.4
7	4.00	6	0.4
8	3.75	7	0.4
9	3.53	8	0.4
10	3.33	9	0.4
11	3.16	10	0.4
12	3.00	11	0.4
13	2.86	12	0.4
14	2.73	13	0.4
15	2.61	14	0.4
16	2.50	15	0.4
17	2.40	16	0.4

For small grazing angles below 0.1 deg, a few more layers are added to each block. For small grazing angles, fewer layers are required by the design scheme. Hence, this result in the bandwidth of each block are broader than 3 keV, which is

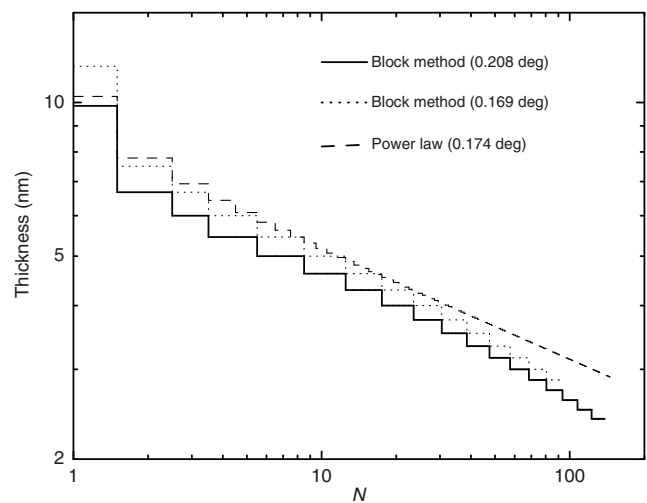


Fig. 12 D -spacing of i 'th layer pair plotted against the layer number from the surface. Solid line shows the design for grazing angle of 0.208 deg shown in Table 1. The design for 0.169 deg (dotted line) and power-law type design (dashed line) also plotted for comparison.

the optimal value derived earlier in the case of 0.208 deg. By adding extra layers, the bandwidth would be reduced to match the energy step ΔE of 3 keV. Furthermore, these additional layers enhance the peak reflectivity R_p so that the integrated reflectivity is improved within the boundary conditions.

The profiles shown in Fig. 12 are step functions obtained from the power-law type of supermirror design. The power-law profiles in this figure are designed for the largest grazing angle (0.174 deg) of the Pt/C multilayer in NuSTAR.¹² The profiles of the block method for a grazing angle of 0.169 deg are also shown for comparison. It is very interesting to find such similarity between two parameter sets derived based on two different design principles.

5 Multilayer Evaluation

The multilayer supermirrors were produced with a DC sputtering system controlled to fabricate them according to the design mentioned in Sec. 4.6. In the production process, the deposition parameters of DC sputtering are tuned based upon x-ray measurements of fiducial multilayer samples created to monitor their changes over time.

The performance of the multilayer supermirrors was measured also with x-rays by changing the grazing angles at a certain mono-energetic x-ray beam or by changing the grazing x-ray beam energy at a certain grazing angle. The reflectivity profile against the grazing angles is characterized by a gradual decrease around the critical angle and a sharp Bragg peak (Fig. 2). The measured first Bragg peak energy determines the multilayer spacing d based on the following equation:

$$m\lambda = 2d \sin \theta (1 - 2\delta/\sin^2 \theta)^{1/2}, \quad (2)$$

where $\delta = 1 - n$ and n is the real part of the refraction index. Furthermore, the measured reflectivity of the first peak determines the interfacial roughness. These parameters, d and roughness, are determined by comparison of the measured profile to that of a simulation with assumed parameters.

The design of the supermirrors was validated by x-ray measurements at Cu $K\alpha$ emission (at $E = 8.0$ keV) with varying grazing angles at our beamline facility in Nagoya University. The multilayer structure, designed for several tens of keV in energy, also produces reflectivity profiles at larger grazing angles for 8 keV according to the same Bragg condition. Only the difference between 8 keV and hard x-rays of 10 to 80 keV measurements is the penetration depth of x-rays. At 8 keV, the upper layers are measured; however, the lower layers must be examined with hard x-rays at several tens of keV. Therefore, these supermirrors were also measured at various x-ray energies with a SPring-8 synchrotron beam facility. The beam produces the energy range from 5 to 113 keV at BL-20B2 with strong and stable (the fluctuation of the ring current is in the order of 10^{-3}) intensity and high parallelism at a distance of 215 m from the light source, or say, 10 arc sec, for a beam size of 10 mm. An energy resolution $E/\Delta E$ of $\sim 10^4$ is provided by a Si double-crystal monochromator. The details are described by Ogasaka et al.¹⁶

The performance of the reflectors for the Hitomi's HXT was also measured in the SPring-8 facility. Figure 13 shows the measured reflectivity of the HXT reflector designed for nominal grazing angle of 0.09 deg at the energy of 30 keV. As shown, the measured reflectivity profile matched well with the simulation. Likewise, the reflectivity at 60 keV can be

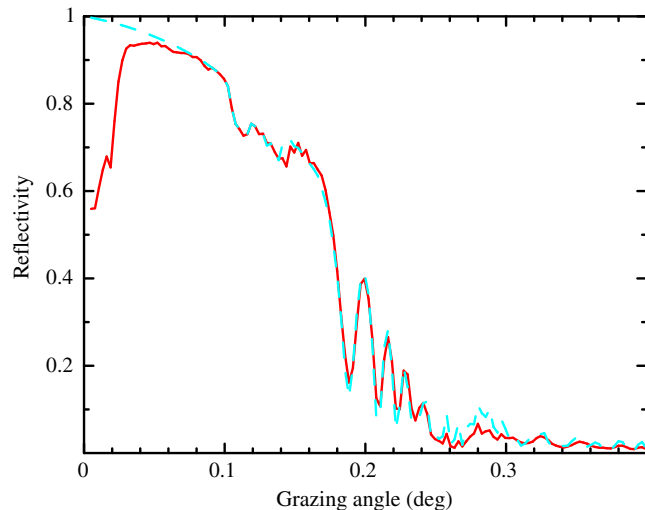


Fig. 13 Reflectivity of supermirror (nominal grazing angle is 0.09 deg) versus grazing angles with 30 keV x-rays at SPring-8. Red solid line shows the actual data, and the dashed line shows a corresponding model expected from the supermirror design.

estimated from the model parameters obtained with 30-keV measurement.

Because the flight mirrors are fabricated using a replication method, the interfacial roughness is strongly affected by the surface roughness of the mandrel. The average interfacial roughness σ ranges from 0.3 to 0.4 nm for the flight mirrors produced so far.

6 Discussion and Summary

Our supermirror design is developed based on the method used in the balloon-borne telescope.⁶ The upper limit of the energy band is extended to 80 keV, and the reflectivity curve is smoothly connected to the total reflection in the lower energy band.

In the earlier development of the block method, the number of bilayers in a block was determined to achieve a target value of reflectivity; in this method, however, we determine the number of bilayers from the saturation curve of the block.

In a comparison with the design used in NuSTAR, some parameters, including d_{\min} , d_{\max} , and the thickness of the top layer, are similar to ours.

The design scheme described in this paper could achieve the scientific requirements of the Hitomi mission. However, there are small-scale ripple structures in the x-ray response of the individual supermirrors. Although they could be smoothed out by adding the responses of many reflectors, such a complex structure must be removed, if possible, in the multilayer design. Additional tuning of the supermirror design by our block method can make the response flatter. In particular, manipulating the thickness of the top several layers will reduce the dips between the total reflection part and the first Bragg peak in the x-ray reflectivity profile. Yao et al.¹⁷ demonstrated a design method to smooth the reflectivity curve profile of a supermirror. This may help us achieve a more efficient design in the future.

Several design schemes we used are customized for the requirements of the Hitomi HXT. The supermirror design has to be optimized to maximize the integrated reflectivity below 10 keV for the example Fe-K band. Under different requirements, some approximations may not work or may require

modification. A combination of different science requirements and technology improvements may lead to better design parameters. Owing to its high flexibility, the block method can be applied to suit different requirements.

Acknowledgments

The basic idea of the multilayer design scheme was first summarized in a master's thesis by Satake in 2004. The developments of the supermirror described in this paper were partly supported by a Grant-in-Aid for Scientific Research, No. 15H02070 (The principal researcher is Awaki). We would like to express our sincere gratitude toward those who contributed to the development of the Hitomi HXT but could not be mentioned in this publication.

References

1. P. J. Serlemitsos et al., "The x-ray telescope on board ASCA," *Publ. Astron. Soc. Jpn.* **47**, 105–114 (1995).
2. H. Kunieda et al., "X-ray telescope onboard Astro-E: optical design and fabrication of thin foil mirrors," *Appl. Opt.* **40**, 553–564 (2001).
3. P. Serlemitsos et al., "The x-ray telescope onboard Suzaku," *Publ. Astron. Soc. Jpn.* **59**, S9–S21 (2007).
4. B. D. Ramsey et al., "First images from hero, a Hard X-Ray Focusing Telescope," *Astrophys. J.* **568**, 432–435 (2002).
5. K. D. Joensen et al., "Design of grazing-incidence multilayer supermirrors for hard-x-ray reflectors," *Appl. Opt.* **34**(34), 7935–7944 (1995).
6. K. Yamashita et al., "Supermirror hard-x-ray telescope," *Appl. Opt.* **37**(34), 8067–8073 (1998).
7. F. Mezei and P. A. Dagleish, "Corrigendum and first experimental evidence on neutron supermirror," *Commun. Phys.* **2**, 41 (1977).
8. J. Tueller et al., "InFOCμs hard x-ray imaging telescope," *Exp. Astron.* **20**, 121–129 (2005).
9. T. Okajima et al., "Characterization of the supermirror hard-x-ray telescope for the InFOCμs balloon experiment," *Appl. Opt.* **41**(25), 5417 (2002).
10. Y. Ogasaka et al., "First light of a hard-x-ray imaging experiment: the InFOCμs balloon flight," *Proc. SPIE* **5900**, 59000R (2005).
11. K. K. Madsen et al., "Optimizations of Pt/SiC and W/Si multilayers for the nuclear spectroscopic telescope array," *Proc. SPIE* **7437**, 743716 (2009).
12. F. E. Christensen et al., "Coatings for the NuSTAR mission," *Proc. SPIE* **8147**, 81470U (2011).
13. H. Matsumoto et al., "Inorbit performance of the hard x-ray telescope (HXT) on board the Hitomi (Astro-H) satellite," *J. Astron. Telec. Instrum. Syst.* (2018), in press.
14. H. Mori et al., "On-ground calibration of the Hitomi hard x-ray telescopes," *J. Astron. Telec. Instrum. Syst.* (2018), in press.
15. T. Takahashi et al., "The Astro-H mission," *Proc. SPIE* **7732**, 77320Z (2010).
16. Y. Ogasaka et al., "Characterization of a Hard X-Ray Telescope at synchrotron facility SPring-8," *Jpn. J. Appl. Phys.* **47**, 5743–5754 (2008).
17. Y. Yao et al., "Design and fabrication of a supermirror with smooth and broad response for Hard X-Ray Telescopes," *Appl. Opt.* **52**(27), 6824 (2013).

Keisuke Tamura is a designated lecturer at Nagoya University. He received his PhD in science from Osaka University in 1993.

Biographies for the other authors are not available.